IEEE Access
Multidisciplinary ⋮ Rapid Review ⋮ Open Access Journal

Received December 9, 2019, accepted December 30, 2019, date of publication January 3, 2020, date of current version January 10, 2020.

Digital Object Identifier 10.1109/ACCESS.2019.2963689

High-Mobility CoMP Massive MIMO Uplink Transmissions: Channel PSD Analysis and Doppler Spread Suppression

ZHINAN HU AND WEILE ZHANG
School of Electronic and Information Engineering, Xi'an Jiaotong University, Xi'an 710049, China

Corresponding author: Weile Zhang (wlzhang@mail.xjtu.edu.cn)

This work was supported in part by the National Natural Science Foundation of China (NSFC) under Grant 61671366 and Grant 61601058, in part by the Natural Science Basic Research Plan in Shaanxi Province of China under Grant 2016JQ6005, and in part by the Fundamental Research Funds for the Central Universities.

ABSTRACT Coordinated Multi-Point transmission/reception (CoMP) is one of the promising techniques for high-mobility wireless communications systems to increase cell edge user throughput in both uplink and downlink transmission. In this paper, we consider the high-mobility CoMP uplink transmission, where a high-speed terminal (HST) simultaneously transmits signals to multiple base stations (BSs) with angle-domain Doppler shifts compensation. We derive the exact channel power spectrum density (PSD) for uplink CoMP transmissions. The antenna weighting technique is then proposed to suppress the Doppler spread, where an optimization problem is formulated to minimize the maximum Doppler spread among all the BSs. Numerical results are provided to corroborate both the PSD analysis and the superiority of antenna weighting technique.

INDEX TERMS High-mobility communication, coordinated multi-point transmission/reception (CoMP), power spectrum density (PSD), Doppler spread.

I. INTRODUCTION

Over the past few years, orthogonal frequency division multiplexing (OFDM) has become a dominant technique for high-mobility wireless communications [1]. However, the relative motion between transceivers can result in fast time fluctuations of the channel and thus brings severe inter-carrier interference (ICI) due to the multiple Doppler shifts superimposed at receiver [2].

Researchers have widely studied the way to combat the Doppler shifts. For sparse high-mobility scenarios with a few dominating paths, the small-scale uniform circular antenna array (UCA) and uniform linear antenna array (ULA) are adopted to separate the multiple Doppler shifts and eliminate ICI via array beamforming [3]. More recently, researchers resort to the large-scale antenna array [4]–[12] to deal with the richly scattered high-mobility scenarios including tunnels or urban areas. On one hand, for downlink high-mobility transmission, the authors in [9] proposed angle-domain Doppler shifts separation scheme to avoid the complicated time-varying channel estimation. On the other hand, for uplink high-mobility transmission, it has been demonstrated that the harmful effect of Doppler shift can be mitigated by massive MIMO technique [10]. Owing to the angle-domain Doppler shifts compensation technique, the asymptotic scaling law in [10] showed that, the Doppler spread decreases approximately as $1/\sqrt{M}$ when M is sufficiently large (M is the number of transmit antennas). Moreover, the high spatial resolution characteristics of massive MIMO transmissions could combat Doppler spread [7], [13]. Besides, the exact power spectrum density (PSD) of uplink equivalent channel is derived in [11], and an antenna weighting technique is further proposed to reduce the channel time variation. However, the scheme in [11] suffers from severe loss of energy radiation efficiency (ERE) when channel has small angular spread [12]. Then, the authors in [12] proposed an ERE aware Doppler spread suppression scheme, and an antenna selection scheme is further developed to save the RF chains.

In addition, coordinated multi-point (CoMP) technique has also attracted a lot of attentions during the past few years [14]. CoMP transmission and reception allow geographically separated BSs to cooperate with each other during

The associate editor coordinating the review of this manuscript and approving it for publication was Matti HäMäLäInen.

the transmission and reception, such that each terminal can be served by multiple base stations (BS) simultaneously. It is seen that the CoMP technique enables (coherent) inter-cell energy combining, interference nulling, spatial utilization improving as well as dead zone covering. Especially, in the context of high-mobility communications, a few works have proposed handover strategies by using the CoMP structure. For example, the work in [15] proposed a CoMP-based soft handover strategy for high-speed railway systems. The handover strategy allows the train to be served by two adjacent BSs with CoMP when the train travels through the overlapping area. The authors in [16] further proposed the idea of sequentially selecting a subset of CoMP BSs to maximize the system capacity. Moreover, a parallel successive convex approximation-based algorithm is introduced for optimal operating point in MIMO CoMP network [17]. The authors in [18] propose an artificial neural network (ANN) MIMO demultiplexer for small cell millimeter-wave radio-over-fiber (RoF) system which improved the system capacity and synchronization tolerance between two adjacent remote radio units (RRUs). A generalized compensated QR decomposition (CQRD) combination scheme with a joint sorting strategy is proposed, which can be applied to scenarios with more than two coordinated BSs [19]. However, to the best of our knowledge, no study has been reported on Doppler spread suppression for high-mobility CoMP transmission.

In this paper, we propose an angle-domain Doppler shifts compensation scheme to reduce the channel time variation for the CoMP uplink transmissions. The channel PSD and the Doppler spread is derived for CoMP uplink transmission. The antenna weighting technique is then proposed to suppress the Doppler spread among all the BSs. Simulation results are provided to verify the proposed scheme. In summary, the new contribution of this paper is twofold:

- We derive the exact channel PSD as well as the Doppler spread for the CoMP uplink transmissions, which differs a lot from the conventional single-BS scenarios [11], [12].
- The antenna weighting technique is then proposed to suppress the Doppler spread, where an optimization problem is formulated to minimize the maximum Doppler spread among all the BSs. Here, the maintenance of transmission ERE is also considered in the optimization problem. Note that the performance balance among the multiple BSs is the main concern of this work. This differs a lot from [12] which considered only one BS.

The remainder of this paper is organized as follows. The system model is presented in Section II. Section III provides the channel PSD analysis for CoMP uplink transmissions. The Doppler spread and transmission ERE is investigated in Section IV. The proposed ERE aware Doppler spread suppression scheme is developed in Section V. Simulation results are provided in Section VI. Section VII concludes the paper.

Notations: Superscripts $(\cdot)^*$, $(\cdot)^T$ and $(\cdot)^H$ represent conjugate, transpose and Hermitian, respectively; $E[\cdot]$ denotes expectation; $\|\cdot\|$ denotes the Frobenius norm operator; $\mathrm{Re}(\cdot)$ denotes the real part; $Tr(\cdot)$ denotes the trace operation; $\mathbb{C}^{m\times n}$ defines the vector space of all $m \times n$ complex matrices.

II. SYSTEM MODEL

We consider the high-mobility uplink CoMP transmission with multiple BSs. For simplicity, the uplink transmission from a HST to two BSs (referred to as BS1 and BS2) is considered as shown in Fig. 1, where an M-element uniform linear array (ULA) is equipped at HST and each BS only have one antenna. Nevertheless, we should note that the discussions can be directly applied to the case with a multi-antenna BS. In a typical scenario where BS is equipped with a co-located antenna array, the ULA at HST would share a common angle of departures (AoD) with the multiple antennas at BS. In this situation, the uplink equivalent channels at each receive antenna should exhibit exactly the same feature of PSD as well as the Doppler spread.

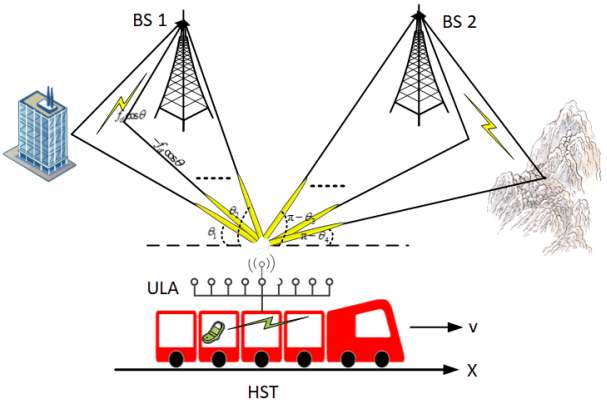

FIGURE 1. Uplink CoMP transmission with high-mobility terminals.

Moreover, when the number of antennas M is massive, channels between different users tend to be orthogonal, and the time-varying channel can be decomposed into a set of parallel time-invariant channels [10], [11]. However, the number of antennas may not be sufficiently large in practice, in which case there will still be uncompensated Doppler shifts due to limited spatial resolution while a thorough time-invariant equivalent channel cannot be achieved for each beamforming branch. The Doppler spread could be employed here as a metric to measure the residual channel time variation [11].

Denote the normalized antenna spacing of ULA as d, which is the ratio between the antenna spacing and the radio wavelength. Denote $a(\theta) = [1, e^{j2\pi d\cos\theta}, \ldots, e^{j2\pi d(M-1)\cos\theta}]^T \in \mathbb{C}^{M\times 1}$ as the array response vector for direction θ. We assume both BS1 and BS2 have only one antenna. We consider the flat fading channel for simplicity. Nevertheless, the proposed scheme can be directly applied to frequency selective channels. In frequency selective

channels, the complex amplitude of each tap varies with time due to multiple Doppler shifts. It is a common assumption that the multiple channel taps are uncorrelated with each other [10]. Therefore, the time variation characteristic of each tap, i.e., the channel PSD and Doppler spread, can be obtained exactly in the same way as the flat fading channel provided in [10]. Specifically, the channel from HST to each BS is composed of a bunch of propagation paths. We assume the AoDs for BS 1 of these paths are constrained within regions of (θ_1, θ_2) while the AoDs for BS2 are constrained within regions of (θ_3, θ_4) [12]. In the following, for ease of presentation, we consider the case of $\theta_3 \geq \theta_2$. Nevertheless, the proposed discussions can be directly applied to the more general cases.

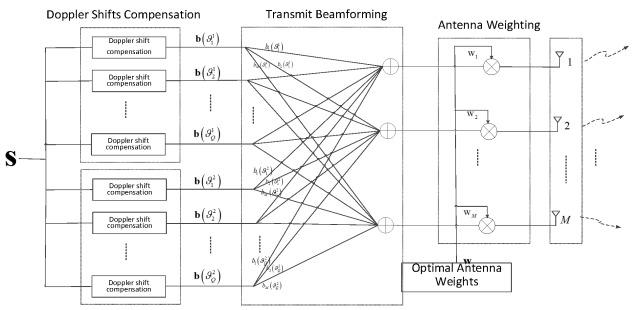

FIGURE 2. Illustration of the transmitter design scheme.

The transmission scheme with angle-domain Doppler shifts compensation is shown in Fig. 2. Denote $s = [s(0), s(1), \ldots, s(N-1)]^T$ as the length-N transmitted time domain symbols in one OFDM block. We consider that the HST simultaneously transmits the symbols s to both the two BSs during the uplink, such that the latter could further perform CoMP reception, e.g., inter-cell energy combining.

Let $\Phi(\epsilon) = \text{diag}(1, e^{j\omega_d T_s \epsilon}, \cdots, e^{j\omega_d T_s (N-1)\epsilon})$ represent the $N \times N$ diagonal phase rotation matrix with $\omega_d = 2\pi f_d$. Here, the frequency shift is $f_d \epsilon$ and T_s is the sampling interval. The multi-branch transmit matched filtering (MF) beamforming is performed towards a set of $2Q$ selected directions: $\vartheta_q^1 \in (\theta_1, \theta_2)$ for BS1 and $\vartheta_q^2 \in (\theta_3, \theta_4)$ for BS2, $q = 1, 2, \ldots, Q$. The qth MF beamformer pointing to BSi can be expressed as

$$b(\vartheta_q^i) = \frac{1}{M\sqrt{Q}} \cdot a(\vartheta_q^i) e^{j\pi\phi(\vartheta_q^i)}. \tag{1}$$

Here, $\phi(\vartheta_q^i)$ denotes an artificial random phase, which is introduced to ensure the time stationary of the uplink equivalent channel at BSs [10].

After Doppler shift compensation, the transmitted $M \times N$ signal matrix at transmit antenna array for the beamforming branch of θ_q^i can be expressed as

$$X_q^i = \text{diag}(w) b^*(\vartheta_q^i) s^T \Phi(-\cos\vartheta_q^i). \tag{2}$$

Here, $w = [w_1, w_2, \cdots, w_M]^T \in \mathbb{C}^{M\times 1}$ denotes the weighting vector, which will be optimized in Section IV.

Next, we first focus on the received signal at BS1. By ignoring the noise item, the received length-N time-domain signal at BS1 can be expressed in the form of

$$\begin{aligned} r &= \sum_{i=1}^{2}\sum_{q=1}^{Q}\int_{\theta_1}^{\theta_2} \alpha(\theta) e^{j\varphi(\theta)} a(\theta)^T X_q^i \Phi(\cos\theta) d\theta \\ &= \sum_{i=1}^{2}\sum_{q=1}^{Q}\int_{\theta_1}^{\theta_2} \alpha(\theta) e^{j\varphi(\theta)} a(\theta)^T \text{diag}(w) b^*(\vartheta_q^i) \\ &\quad \times s^T \Phi(-\cos\vartheta_q^i) \Phi(\cos\theta) d\theta, \end{aligned} \tag{3}$$

where $\alpha(\theta)$ and $\varphi(\theta)$ denote the random gain and phase of the channel propagation path associated with AoD θ, respectively.

III. CHANNEL PSD ANALYSIS

According to (3), the continuous-time form of the equivalent uplink channel at BS1 can be expressed as

$$\begin{aligned} g(t) = \frac{1}{\sqrt{Q}} \sum_{i=1}^{2}\sum_{q=1}^{Q}\int_{\theta_1}^{\theta_2} \alpha(\theta) G(\cos\theta, \cos\vartheta_q^i) \\ \times e^{j\omega_d t\cos\theta - j\omega_d t\cos\vartheta_q^i + j\varphi(\theta) - j\phi(\vartheta_q^i)} d\theta, \end{aligned} \tag{4}$$

where

$$\begin{aligned} G(\cos\theta, \cos\vartheta_q^i) &= \frac{1}{M} a^H(\vartheta_q^i) \text{diag}(w) a(\theta) \\ &= \frac{1}{M}\sum_{r=1}^{M} w_r e^{j2\pi d(r-1)(\cos\theta - \cos\vartheta_q^i)}. \end{aligned} \tag{5}$$

The autocorrelation for the equivalent continuous channel $g(t)$ can be then given by

$$\begin{aligned} R_g &= E\big[g(t) g^*(t+\tau)\big] \\ &= \frac{1}{Q}\sum_{j=1}^{2}\sum_{i=1}^{2}\sum_{q=1}^{Q}\sum_{k=1}^{Q}\int_{\theta_1}^{\theta_2}\int_{\theta_1}^{\theta_2} E\big[\alpha(\theta)\alpha^*(\tilde{\theta}) e^{j[\varphi(\theta)-\varphi(\tilde{\theta})]} \\ &\quad \times e^{j[\phi(\vartheta_k^j)-\phi(\vartheta_q^i)]} G(\cos\theta, \cos\vartheta_q^i) G^*(\cos\tilde{\theta}, \cos\vartheta_k^j) \\ &\quad \times e^{j\omega_d(\cos\theta - \cos\vartheta_q^i)t - j\omega_d(\cos\tilde{\theta} - \cos\vartheta_k^j)(t+\tau)}\big] d\theta d\tilde{\theta} \\ &\doteq \frac{1}{Q}\sum_{i=1}^{2}\sum_{q=1}^{Q}\int_{\theta_1}^{\theta_2} E\big[|\alpha(\theta)|^2\big] |G(\cos\theta, \cos\vartheta_q^i)|^2 \\ &\quad \times e^{-j\omega_d(\cos\theta - \cos\vartheta_q^i)\tau} d\theta, \\ &\doteq \frac{1}{(\theta_2 - \theta_1)Q}\sum_{i=1}^{2}\sum_{q=1}^{Q}\int_{\theta_1}^{\theta_2} |G(\cos\theta, \cos\vartheta_q^i)|^2 \\ &\quad \times e^{-j\omega_d(\cos\theta - \cos\vartheta_q^i)\tau} d\theta, \end{aligned} \tag{6}$$

and $\doteq$ employs the properties

$$E\big[e^{j[\varphi(\theta)-\varphi(\tilde{\theta})]}\big] = \begin{cases} 1, & \theta = \tilde{\theta} \\ 0, & \theta \neq \tilde{\theta}, \end{cases}$$

$$E\big[e^{j[\phi(\vartheta_k^i)-\phi(\vartheta_q^j)]}\big] = \begin{cases} 1, & q = k \text{ and } i = j, \\ 0, & \text{otherwise.} \end{cases}$$

and $\ddot{=}$ is due to

$$E\left[|\alpha(\theta)|^2\right] = \frac{1}{\theta_2 - \theta_1}.$$

The explicit expression of the channel PSD at BS1, which is the Fourier transform of the channel autocorrelation $R_g(\tau)$, is given in the following:

$$\begin{aligned} P(\omega) &= \int_{-\infty}^{+\infty} R_g(\tau) e^{-j\omega\tau} d\tau \\ &= \frac{1}{(\theta_2-\theta_1)Q} \sum_{i=1}^{2}\sum_{q=1}^{Q} \int_{\theta_1}^{\theta_2} |G(\cos\theta, \cos\vartheta_q^i)|^2 \\ &\quad \times \left[\int_{-\infty}^{+\infty} e^{-j\omega_d(\cos\theta - \cos\vartheta_q^i)\tau} e^{-j\omega\tau} d\tau\right] d\theta \\ &= \frac{2\pi}{(\theta_2-\theta_1)Q} \sum_{i=1}^{2}\sum_{q=1}^{Q} \int_{\theta_1}^{\theta_2} |G(\cos\theta, \cos\vartheta_q^i)|^2 \\ &\quad \times \delta(\omega + \omega_d(\cos\theta - \cos\vartheta_q^i)) d\theta, \end{aligned} \tag{7}$$

where we have exploited the following equality:

$$\int_{-\infty}^{+\infty} e^{-j\omega_d(\cos\theta - \cos\vartheta_q^i)\tau} e^{-j\omega\tau} d\tau = 2\pi\delta(\omega + \omega_d(\cos\theta - \cos\vartheta_q^i)).$$

By defining

$$\chi(x, y) = \cos x + y$$

there holds the formula in (8), as shown at the bottom of this page.

Let $S_i(\tilde{\omega})$ stand for the index set of beamforming branches contributing to the PSD at $\tilde{\omega}$. There hold:

$$\begin{aligned} S_1(\tilde{\omega}) = \{q | &\chi(\theta_2, \tilde{\omega}) \le \cos\vartheta_q^1 \le \chi(\theta_1, \tilde{\omega}), \\ &\cos\theta_1 \le \cos\vartheta_q^1 \le \cos\theta_2\}, \end{aligned} \tag{9}$$

$$\begin{aligned} S_2(\tilde{\omega}) = \{q | &\chi(\theta_2, \tilde{\omega}) \le \cos\vartheta_q^2 \le \chi(\theta_1, \tilde{\omega}), \\ &\cos\theta_3 \le \cos\vartheta_q^2 \le \cos\theta_4\}. \end{aligned} \tag{10}$$

Combining the above formula with (7), the PSD is obtained as follows

$$\begin{aligned} P(\omega) &= \frac{2\pi}{(\theta_2-\theta_1)Q} B(\tilde{\omega}) \sum_{i=1}^{2}\sum_{q=1}^{Q} \frac{1}{\omega_d} \frac{1}{\sqrt{1-\chi(\vartheta_q^i, -\tilde{\omega})^2}} \mathcal{I}_q^i(\tilde{\omega}) \\ &= \frac{1}{\omega_d} B(\tilde{\omega}) \sum_{i=1}^{2} W_i(\tilde{\omega}). \end{aligned} \tag{11}$$

where

$$B(\tilde{\omega}) = |\frac{1}{M} \boldsymbol{v}_i{}^T(\tilde{\omega}) w|^2 = |\frac{1}{M} \sum_{r=1}^{M} w_r e^{-j2\pi d(r-1)\tilde{\omega}}|^2, \tag{12}$$

$$W_i(\tilde{\omega}) = \frac{2\pi}{(\theta_2-\theta_1)Q} \sum_{q=1}^{Q} \frac{1}{\sqrt{1-\chi(\vartheta_q^i, -\tilde{\omega})^2}} \mathcal{I}_q^i(\tilde{\omega}),$$

$$\mathcal{I}_q^i(\tilde{\omega}) = \begin{cases} 1, & q \in S_i(\tilde{\omega}) \\ 0, & q \notin S_i(\tilde{\omega}) \end{cases} \tag{13}$$

It can be observed that, $B(\tilde{\omega})$ is the scaled radiation pattern obtained from the antenna weighted MF beamformer pointing to the normal direction. Hence, $B(\tilde{\omega})$ is named as beam function. On the other side, $W_i(\tilde{\omega})$, $i = 1, 2$, represent the impact of different beamformers on the PSD and are named as window functions to highlight its distortion effect on the beam function $B(\tilde{\omega})$.

Next, we consider the following typical configurations of beamforming directions [11]: $\cos\vartheta_q^1, q = 1, 2, \ldots, Q$ are evenly distributed between $(\cos\theta_1, \cos\theta_2)$ and $\cos\vartheta_q^2, q = 1, 2, \ldots, Q$ are evenly distributed between $(\cos\theta_3, \cos\theta_4)$. In this situation, denote

$$\mu(\theta_1, \theta_2) = \cos\theta_1 - \cos\theta_2, \tag{14}$$

and a more concise form for function function $W_1(\tilde{\omega})$ can be directly obtained from [11], that is

$$\begin{aligned} &W_1(\tilde{\omega}) \\ &= \begin{cases} \frac{2\pi}{(\theta_2-\theta_1)} \frac{\arccos(\cos\theta_2 - \tilde{\omega}) - \theta_1}{\mu(\theta_1, \theta_2)}, & -\mu(\theta_1, \theta_2) \le \tilde{\omega} < 0 \\ \frac{2\pi}{(\theta_2-\theta_1)} \frac{\theta_2 - \arccos(\cos\theta_1 - \tilde{\omega})}{\mu(\theta_1, \theta_2)}, & 0 \le \tilde{\omega} \le \mu(\theta_1, \theta_2) \end{cases} \end{aligned} \tag{15}$$

However, the further simplification of $W_2(\tilde{\omega})$ is quite different from $W_1(\tilde{\omega})$, whose derivation is given as Appendix.

After the variable substitution, $W_2(\tilde{\omega})$ can be finally expressed in closed-form as (16-1) and (16-2), as shown at the bottom of the next page. As an illustration example, we depict different cases of window function in Fig. 3. The following two cases are considered: (1). Case I: $\theta_1 = 10°, \theta_2 = 40°, \theta_3 = 50°, \theta_4 = 80°$ and (2). Case II: $\theta_1 = 10°, \theta_2 = 40°,$

$$\begin{aligned} &\int_{\theta_1}^{\theta_2} |G(\cos\theta, \cos\vartheta_q^i)|^2 \delta(\omega + \omega_d(\cos\theta - \cos\vartheta_q^i)) d\theta \\ &\overset{y=\omega_d\cos\theta}{=} \frac{1}{\omega_d} \int_{\omega_d\cos\theta_2}^{\omega_d\cos\theta_1} |G(\frac{y}{\omega_d}, \cos\vartheta_q^i)|^2 \frac{1}{\sqrt{1-(\frac{y}{\omega_d})^2}} \delta(y + \omega - \omega_d\cos\vartheta_q^i) dy \\ &= \begin{cases} \frac{1}{\omega_d} |G(\chi(\vartheta_q^i, -\frac{\omega}{\omega_d}), \cos\vartheta_q^i)|^2 \frac{1}{\sqrt{1-\chi(\vartheta_q^i, -\frac{\omega}{\omega_d})^2}}, & -\cos\theta_1 \le \frac{\omega}{\omega_d} - \cos\vartheta_q^i \le -\cos\theta_2 \\ 0, & \textit{otherwise}, \end{cases} \\ &\overset{\tilde{\omega}=\frac{\omega}{\omega_d}}{=} \begin{cases} \frac{1}{\omega_d} |\mathcal{G}_i(\tilde{\omega})|^2 \frac{1}{\sqrt{1-\chi(\vartheta_q^i, -\tilde{\omega})^2}}, & -\cos\theta_1 \le \tilde{\omega} - \cos\vartheta_q^i \le -\cos\theta_2 \\ 0, & \textit{otherwise} \end{cases} \end{aligned} \tag{8}$$

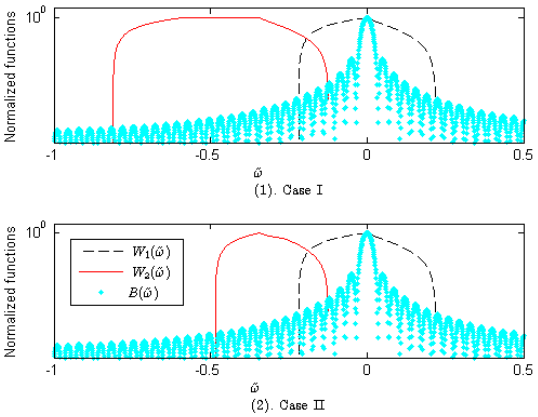

FIGURE 3. Comparison of the window functions $W(\tilde{\omega})$ and beam function $B(\tilde{\omega})$ in two cases.

$\theta_3 = 50°, \theta_4 = 60°$, which correspond to $\mu(\theta_3,\theta_4) > \mu(\theta_1,\theta_2)$ and $\mu(\theta_3,\theta_4) < \mu(\theta_1,\theta_2)$, respectively.

IV. DOPPLER SPREAD AND ENERGY RADIATION EFFICIENCY ANALYSIS

According to the above discussion, the PSD proves to be determined by both the beam function and window function. Thus it is possible to reduce the Doppler spread by modifying the beam function, which in fact corresponds to the radiation pattern of array. Specifically, the weights w could be optimized to minimize the Doppler spread, which is equivalent to reduce the residual time variation of the channel.

As a result, the Doppler spread with antenna weighting at BS1 can be calculated as

$$\begin{aligned}\sigma_{DS} &= \sqrt{\frac{\int_{-\infty}^{+\infty}\omega^2 P(\omega)d\omega}{\int_{-\infty}^{+\infty}P(\omega)d\omega}} \\ &\overset{\omega=\omega_d\tilde{\omega}}{=} \omega_d\sqrt{\frac{\int_{-\infty}^{+\infty}\tilde{\omega}^2(\sum_{i=1}^{2}|\boldsymbol{\nu}^T(\tilde{\omega})w|^2W_i(\tilde{\omega}))d\omega}{\int_{-\infty}^{+\infty}(\sum_{i=1}^{2}|\boldsymbol{\nu}^T(\tilde{\omega})w|^2W_i(\tilde{\omega}))d\tilde{\omega}}} \\ &= \omega_d\sqrt{\frac{w^HC_2w}{w^HC_0w}}. \end{aligned} \tag{17}$$

where

$$\boldsymbol{\nu}(\tilde{\omega}) = [1, e^{-j2\pi d\tilde{\omega}}, \ldots, e^{-j2\pi d(M-1)\tilde{\omega}}]^T, \tag{18}$$

$$\begin{aligned}C_2^1 = &\int_{-\mu(\theta_1,\theta_2)}^{\mu(\theta_1,\theta_2)}\tilde{\omega}^2W_1(\tilde{\omega})\boldsymbol{\nu}^*(\tilde{\omega})\boldsymbol{\nu}^T(\tilde{\omega})d\tilde{\omega} \\ &+\int_{-\mu(\theta_1,\theta_4)}^{-\mu(\theta_2,\theta_3)}\tilde{\omega}^2W_2(\tilde{\omega})\boldsymbol{\nu}^*(\tilde{\omega})\boldsymbol{\nu}^T(\tilde{\omega})d\tilde{\omega},\end{aligned} \tag{19}$$

$$\begin{aligned}C_0^1 = &\int_{-\mu(\theta_1,\theta_2)}^{\mu(\theta_1,\theta_2)}W_1(\tilde{\omega})\boldsymbol{\nu}^*(\tilde{\omega})\boldsymbol{\nu}^T(\tilde{\omega})d\tilde{\omega} \\ &+\int_{-\mu(\theta_1,\theta_4)}^{-\mu(\theta_2,\theta_3)}W_2(\tilde{\omega})\boldsymbol{\nu}^*(\tilde{\omega})\boldsymbol{\nu}^T(\tilde{\omega})d\tilde{\omega}.\end{aligned} \tag{20}$$

Then, the normalized Doppler spread for BS1 can be defined as

$$\frac{\sigma_D}{\omega_d} = \sqrt{\frac{w^HC_2^1w}{w^HC_0^1w}}, \tag{21}$$

which represents the magnitude of Doppler spread suppression benefiting from the angle-domain Doppler shifts compensation scheme.

Although antenna weighting can minimize Doppler spread, it may lead to severe loss of transmission efficiency [12]. In order to reduce the leakage of radiation efficiency, the ERE is also need to be considered, which can be defined as $\frac{w^HC_0^1w}{w^Hw}$ for BS1 [12].

TABLE 1. Normalized doppler spread and ERE under different BSs.

	normalized Doppler spread	ERE
BS1	$\sqrt{\frac{w^HC_2^1w}{w^HC_0^1w}}$	$\frac{w^HC_0^1w}{w^Hw}$
BS2	$\sqrt{\frac{w^HC_2^2w}{w^HC_0^2w}}$	$\frac{w^HC_0^2w}{w^Hw}$

Following the similar steps as above, we can perform the analysis of Doppler spread and ERE for BS2. In summary, we list the normalized Doppler spread and ERE for two BSs in Table 1. The expression of C_0^2 and C_2^2 for BS2 have the same form as C_2^1 and C_0^1 in (19) and (20) with replacing θ_1, θ_2 by θ_3, θ_4, respectively.

Case $\mu(\theta_3,\theta_4) > \mu(\theta_1,\theta_2)$:

$$W_2(\tilde{\omega}) = \begin{cases}\dfrac{2\pi}{(\theta_2-\theta_1)}\dfrac{\theta_2 - arccos(cos\theta_3-\tilde{\omega})}{\mu(\theta_3,\theta_4)}, & -\mu(\theta_1,\theta_3) \le \tilde{\omega} < -\mu(\theta_2,\theta_3) \\ \dfrac{2\pi}{(\theta_2-\theta_1)}\dfrac{\theta_2-\theta_1}{\mu(\theta_3,\theta_4)}, & -\mu(\theta_2,\theta_4) \le \tilde{\omega} < -\mu(\theta_1,\theta_3) \\ \dfrac{2\pi}{(\theta_2-\theta_1)}\dfrac{\arccos(cos\theta_4-\tilde{\omega})-\theta_1}{\mu(\theta_3,\theta_4)}, & -\mu(\theta_1,\theta_4) \le \tilde{\omega} \le -\mu(\theta_2,\theta_4)\end{cases} \tag{16-1}$$

Case $\mu(\theta_3,\theta_4) \le \mu(\theta_1,\theta_2)$:

$$W_2(\tilde{\omega}) = \begin{cases}\dfrac{2\pi}{(\theta_2-\theta_1)}\dfrac{\theta_2 - arccos(cos\theta_3-\tilde{\omega})}{\mu(\theta_3,\theta_4)}, & -\mu(\theta_2,\theta_4) \le \tilde{\omega} < -\mu(\theta_2,\theta_3) \\ \dfrac{2\pi}{(\theta_2-\theta_1)}\dfrac{arccos(cos\theta_4-\tilde{\omega})-arccos(cos\theta_3-\tilde{\omega})}{\mu(\theta_3,\theta_4)}, & -\mu(\theta_1,\theta_3) \le \tilde{\omega} < -\mu(\theta_2,\theta_4) \\ \dfrac{2\pi}{(\theta_2-\theta_1)}\dfrac{\arccos(cos\theta_4-\tilde{\omega})-\theta_1}{\mu(\theta_3,\theta_4)}, & -\mu(\theta_1,\theta_4) \le \tilde{\omega} \le -\mu(\theta_1,\theta_3)\end{cases} \tag{16-2}$$

V. ERE AWARE DOPPLER SPREAD SUPPRESSION

In this section, we propose the antenna weighting scheme for uplink CoMP tranmsissions to suppress the Doppler spread among all the BSs. The maintaining of transmission ERE is also taken into consideration in the proposed scheme.

First, we only consider the optimization of ERE. On the one hand, for only considering BS1, the maximum energy radiance efficiency is $\lambda_{\max}(C_0^1)$, where $\lambda_{\max}(\cdot)$ denotes the maximal eigenvalue of given argument. On the other hand, for only considering BS2, the maximum energy radiance efficiency is $\lambda_{\max}(C_0^2)$. In the case that the same weighting constraint is considered, we propose the following optimization problem to acquire the maximum possible ERE value for both two BSs.

The normalized ERE can be defined for the BS$i(i = 1, 2)$ as follows:

$$r_i(\tilde{w}) = \frac{\frac{\tilde{w}^H C_0^i \tilde{w}}{\tilde{w}^H \tilde{w}}}{\lambda_{\max}(C_0^i)}. \tag{22}$$

The maximum possible normalized ERE for both two BSs $r_{\max} = \max_{\tilde{w}}(r_i(\tilde{w}), i = 1, 2.$ can be acquired by solving the following optimization problem:

$$\begin{aligned} r_{\max} = \ & \min_{\tilde{w}} \ r, \\ & s.t.\ r_i(\tilde{w}) \geq r, \quad i = 1, 2. \end{aligned} \tag{23}$$

By substituting (22) into (23), we can transfer the problem of (23) into

$$\begin{aligned} r_{\max} = \ & \min_{\tilde{w}} \quad r, \\ & s.t.\ \tilde{w}^H C_0^i \tilde{w} \geq r \cdot \lambda_{\max}(C_0^i), \quad i = 1, 2, \\ & \tilde{w}^H \tilde{w} \leq 1. \end{aligned} \tag{24}$$

Note that the above problem is not a typical convex problem due to the non-convex constraints. We then resort to the SPCA method [20] to solve the above non-convex problem iteratively. Specifically, by given the optimal solution in the lth iteration $\hat{w}_l$ and given a Hermitian matrix X, we know $\tilde{w}^H X \tilde{w}$ is lower bounded by its first Taylor expansion $f(\tilde{w}, \hat{w}_l)$, or mathematically, there holds

$$f_X(\tilde{w}, \hat{w}_l) = \hat{w}_l^H X \hat{w}_l + 2\Re\Big(\mathrm{Tr}\big(\hat{w}_l^H X(\tilde{w} - \hat{w}_l)\big)\Big), \tag{25}$$

Hence, given any scalar a irrelevant to $\tilde{w}$, the feasible set of $f_X(\tilde{w}, \hat{w}_l) \geq a$ serves as a subset of $\tilde{w}^H X \tilde{w} \geq a$.

Then, regarding the problem of (24), given an optimal weighting vector $\hat{w}_l$ in the lth iteration, the optimal solution in the $(l+1)th$ iteration can be obtained by solving the following convex problem:

$$\begin{aligned} r_{\max} = \ & \min_{\tilde{w}} \quad r, \\ & s.t.\ r \cdot \lambda_{\max}(C_0^i) - f_{C_0^i}(\tilde{w}, \hat{w}_l) \leq 0, \quad i = 1, 2, \\ & \tilde{w}^H \tilde{w} - 1 \leq 0. \end{aligned} \tag{26}$$

The above iteration procedure can be simply initialized with $\hat{w}_0 = 1_M$.

Once the maximum possible normalized ERE for both two BSs is obtained, we then turn to the design of ERE aware Doppler spread suppression for CoMP uplink transmissions. Specifically, we formulate the following optimization problem to minimize the maximum Doppler spread of two BSs:

$$\hat{w} = \arg\min_{\tilde{w}} \max\left(\frac{\tilde{w}^H C_2^i \tilde{w}}{\tilde{w}^H C_0^i \tilde{w}}\right), \tag{27a}$$

$$s.t.\ r_i(\tilde{w}) \geq \varepsilon \cdot r_{\max}, \quad i = 1, 2, \tag{27b}$$

where ε is introduced to constrain the loss of the ERE for the two BSs.

Denote $\eta_i = r_{\max} \cdot \lambda_{\max}(C_0^i), i = 1, 2$. We can transform the optimization problem (27) by introducing auxiliary variables s, t:

$$\begin{aligned} \hat{w} = \ & \arg\min_{\tilde{w}} \quad s, \\ & s.t.\ \tilde{w}^H C_2^1 \tilde{w} \leq s, \\ & \quad \tilde{w}^H C_0^1 \tilde{w} \geq 1, \\ & \quad \frac{\tilde{w}^H C_2^2 \tilde{w}}{t} \leq s, \\ & \quad \tilde{w}^H C_0^2 \tilde{w} \geq t, \\ & \quad \tilde{w}^H \tilde{w} - \frac{t}{\varepsilon \cdot \eta_i} \leq 0, \quad i = 1, 2. \end{aligned} \tag{28}$$

Note that $w^H C_0^1 w \geq 1$ and $w^H C_0^2 w \geq t$ are not convex constraints. We then resort to the SPCA method [20] to solve the above non-convex problem iteratively.

Then, the optimal solution in the $(l+1)th$ iteration can be obtained by solving the following convex problem:

$$\begin{aligned} \hat{w}_{l+1} = \ & \arg\min_{\tilde{w}} \quad s, \\ & s.t.\ \tilde{w}^H C_2^1 \tilde{w} \leq s, \\ & \quad 1 - f_{C_0^1}(\tilde{w}, \hat{w}_l) \leq 0, \\ & \quad \frac{\tilde{w}^H C_2^2 \tilde{w}}{t} \leq s, \\ & \quad t - f_{C_0^2}(\tilde{w}, \hat{w}_l) \leq 0, \\ & \quad \tilde{w}^H \tilde{w} - \frac{t}{\varepsilon \cdot \eta_i} \leq 0, \quad i = 1, 2. \end{aligned} \tag{29}$$

Note that the initial feasible solution $\hat{w}_0$ can be found by the concept of Iterative Feasibility Search Algorith (IFSA) algorithm [21]. Specifically, given the optimal weighting vector $\hat{w}_{0,l}$ for $\hat{w}_0$ in the lth iteration, the optimal solution in the $(l+1)th$ iteration can be obtained by the following convex problem:

$$\begin{aligned} \hat{w}_{0,l+1} = \ & \arg\min_{\tilde{w}_0} \quad s_0, \\ & s.t.\ 1 - f_{C_0^1}(\tilde{w}_0, \hat{w}_{0,l}) \leq s_0, \\ & \quad t - f_{C_0^2}(\tilde{w}_0, \hat{w}_{0,l}) \leq s_0, \\ & \quad \tilde{w}_0^H \tilde{w}_0 - \frac{1}{\varepsilon \cdot \eta_1} \leq s_0, \\ & \quad \tilde{w}_0^H \tilde{w}_0 - \frac{t}{\varepsilon \cdot \eta_2} \leq s_0. \end{aligned} \tag{30}$$

VI. SIMULATION RESULTS

In this section, we present simulation results to verify the proposed studies. We consider a ULA with a total of $M = 64$ antennas and the normalized antenna spacing of 0.45. The maximum Doppler shift is set as $f_d = 1000$Hz with the velocity of HST as $v = 360$km/h and the carrier frequency as 3GHz. The beamforming directions are selected such that $\cos\vartheta_q^1$ are evenly distributed between $(\cos\theta_1, \cos\theta_2)$ and $\cos\vartheta_q^2$ are evenly distributed between $(\cos\theta_3, \cos\theta_4)$. For comparison, we include the results of [10], [11] and [12], labelled as "equal weighting", "AW-Mini-DS" and "AW-Mini-DS-ERE", respectively. Note that "equal weighting", "AW-Mini-DS" and "AW-Mini-DS-ERE" only consider a single BS scenario. In the studied CoMP scenario, we let equal weighting, AW-Mini-DS and AW-Mini-DS-ERE optimize the antenna weighting with respect to BS1 or BS2 individually.

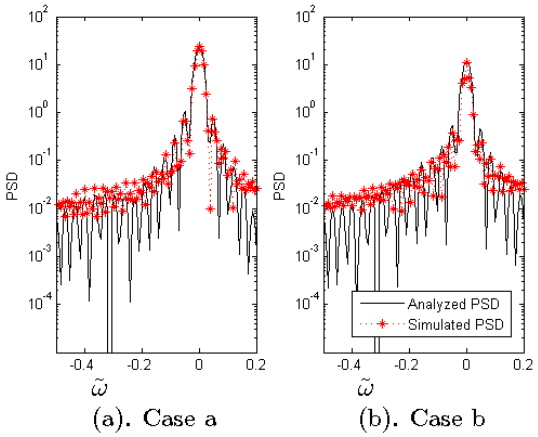

FIGURE 4. Comparison of PSD $P(\tilde{\omega})$ in two cases.

In the first example, the accuracy of the PSD analysis is verified. We compare the channel PSD in Fig. 4 under the following different cases for AoD regions:

(a) Case a: $\theta_1 = 10°, \theta_2 = 60°, \theta_3 = 65°, \theta_4 = 70°$
(b) Case b: $\theta_1 = 10°, \theta_2 = 40°, \theta_3 = 50°, \theta_4 = 70°$

In order to verify the correctness of PSD derivation (11), we provide the numerical PSD obtained in the following way: First the channel autocorrelation $R_g(\tau)$ is calculated at N discrete time points by averaging over sufficient number of channel realizations (3) and then an N-point discrete Fourier transform (DFT) is applied to obtain the discretized PSD. Note that N should be accordingly increased with the number of antennas M to capture the faster fluctuation of the magnitude of the PSD. Fig.4 reveals that for both two cases, the analyzed PSD (11) perfectly coincides with its numerical counterpart, confirming the validity of the PSD analysis.

In Fig. 5, we further include the radiation pattern of the proposed scheme for comparison. The AoD region is $\theta_1 = 10°$, $\theta_2 = 60°, \theta_3 = 60°, \theta_4 = 70°$. As expected, it is observed that the sidelobe level of the proposed scheme is much lower than that of AW-Mini-DS. This intuitively implies that the proposed method should provide much better radiation efficiency for both two BSs than AW-Mini-DS. This verifies that the proposed scheme indeed could maintain radiation efficiency in CoMP.

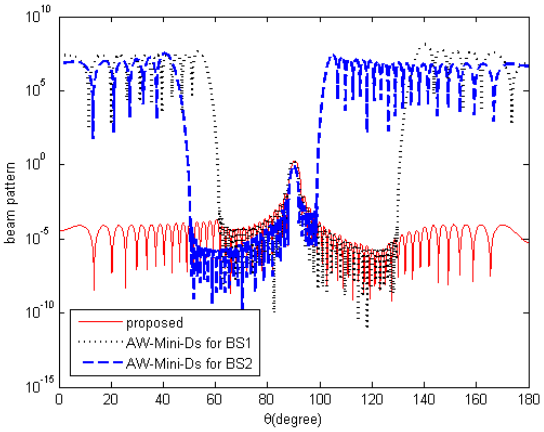

FIGURE 5. Comparison of ERE in different cases.

TABLE 2. Comparison of normalized Doppler spread in different cases.

Normalized Doppler spread / scheme	cases	case1	case2	case3	case4
proposed	BS1	0.0180	0.0133	0.0162	0.0246
	BS2	0.0170	0.0079	0.0150	0.0291
AW-Mini-DS for BS1	BS1	0.0146	0.0108	0.0145	0.0108
	BS2	0.5859	0.7221	0.5868	0.2850
AW-Mini-DS for BS2	BS1	0.3748	0.6368	0.3055	0.5673
	BS2	0.0119	0.0078	0.0093	0.0147
AW-Mini-DS-ERE for BS1	BS1	0.0159	0.0149	0.0158	0.0135
	BS2	0.0544	0.1262	0.0417	0.1766
AW-Mini-DS-ERE for BS2	BS1	0.2299	0.1383	0.1742	0.0378
	BS2	0.0141	0.0114	0.0121	0.0163
equal weighting	BS1	0.0432	0.0366	0.0441	0.0226
	BS2	0.0253	0.0208	0.0191	0.0411

We show the optimization results of normalized Doppler spread and ERE in the proposed scheme in Table 2 and Table 3. The following four different configurations for AoD regions are considered:

- Case 1: $\theta_1 = 40°, \theta_2 = 50°, \theta_3 = 50°, \theta_4 = 80°$
- Case 2: $\theta_1 = 10°, \theta_2 = 60°, \theta_3 = 65°, \theta_4 = 70°$
- Case 3: $\theta_1 = 20°, \theta_2 = 40°, \theta_3 = 80°, \theta_4 = 85°$
- Case 4: $\theta_1 = 10°, \theta_2 = 60°, \theta_3 = 60°, \theta_4 = 70°$

In Table 2, as expected, we can see that all of the equal weighting, AW-Mini-DS and AW-Mini-DS-ERE design antenna weighting for only one BS. Therefore, it is impossible to achieve the effect of reducing the Doppler spread for two BSs simultaneously. In contrast of them, the proposed method consider both two BSs, which would simultaneously reduce the Doppler spread for both two BSs.

In Table 3, the ERE is compared between the proposed method and AW-Mini-DS. Because the ERE is not considered in AW-Mini-DS, the loss of ERE in AW-Mini-DS is very large. The ERE in AW-Mini-DS is almost 0 in one BS when

TABLE 3. Comparison of normalized radiation efficiency in different cases.

Normalized radiation efficiency: scheme \ cases		case1	case2	case3	case4
proposed	BS1	0.700	0.710	0.586	0.887
	BS2	0.985	0.900	0.990	0.647
AW-Mini-DS for BS1	BS1	4.00×10^{-8}	1.34×10^{-7}	7.06×10^{-7}	1.07×10^{-7}
	BS2	0.010	0.084	0.015	0.504
AW-Mini-DS for BS2	BS1	0.353	0.171	0.482	0.006
	BS2	1.05×10^{-8}	1.73×10^{-7}	3.96×10^{-7}	2.81×10^{-7}
AW-Mini-DS-ERE for BS1	BS1	0.500	0.500	0.500	0.500
	BS2	0.742	0.662	0.854	0.575
AW-Mini-DS-ERE for BS2	BS1	0.628	0.563	0.610	0.858
	BS2	0.500	0.500	0.500	0.500
equal weighting	BS1	0.678	0.770	0.583	0.965
	BS2	0.971	0.960	0.962	0.584

the optimization is considered for the other BS. For example, the normalized radiation efficiency in case 1 of BS1 which obtained from 'AW-Mini-DS for BS1' is 4.00×10^{-8}. The normalized energy radiation efficiency is the ratio of the radiation efficiency to the maximum possible radiation efficiency and represents the level of maintained relative radiation efficiency. The normalized radiation efficiency equals 4.00×10^{-8} in AW-Mini-DS in Table 3, which means almost all of the radiation power has leaked out. Conversely, the proposed method takes into account both two BSs and can provide satisfactory ERE closed to the maximum value.

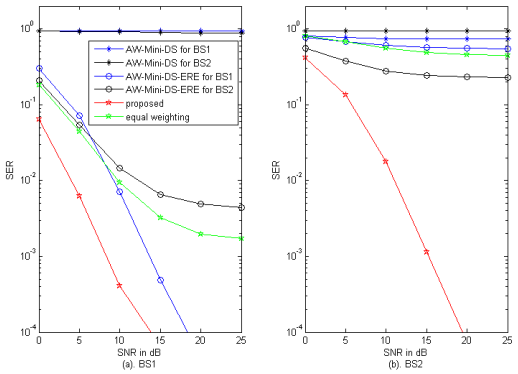

FIGURE 6. Comparison of the SER obtained with different schemes.

Fig. 6 compares the symbol error rate (SER) performance for BS1 and BS2 obtained with the received signals after optimal antenna weighting with different schemes. We consider the receiver employs a 4-element ULA with the normalized antenna spacing $d = 0.5$ and maximum-ratio-combining (MRC) is used to detect the data symbols. Each OFDM frame consists of 5 blocks, with the first block serving as pilot block. The number of subcarriers is taken as 128, and both pilot and data symbols are randomly drawn from 16-QAM constellation. The block duration is assumed to be $T_b = 0.1$ms. We assume the Jakes channel model between the BS and the moving terminal as in [22]. The tap number of the channel is 6 with 64 paths in each tap and the maximum channel delay is 16. Besides, we choose AoD regions in case 1. From Fig. 6, the SER performance is determined by the optimal weighting in different schemes. The superiority of the proposed optimal antenna weighting technique is evident. Moreover, the radiation efficiency directly reflects the channel gain of the uplink transmissions, and the Doppler spread suppression reflects the suppression effect of the uplink channel time variation. As expected, the SER performance with proposed scheme does not exhibit obvious floor and is better than equal weighting, AW-Mini-DS and AW-Mini-DS-ERE. This is due to the fact that the proposed scheme can substantially reduce the Doppler spread and enhance the radiation efficiency, compared to equal weighting, AW-Mini-DS and AW-Mini-DS-ERE.

VII. CONCLUSION

In this paper, we consider the angle-domain Doppler shifts compensation scheme for high-mobility uplink CoMP communication. The exact PSD is derived for uplink CoMP scenario. The antenna weighting technique is proposed to suppress the Doppler spread and consider the maintenance of transmission ERE among all BSs. There are two important indicators we need to consider: Doppler spread and energy radiation efficiency. Then we have formulated an optimization problem which tries to minimize the maximal Doppler spreads of the two BSs given the constraint of ERE maintenance. Note that the above optimization problem is not a typical convex problem due to the non-convex constraints. We then resort to the SPCA method [20] to solve the above non-convex problem iteratively. Due to nonconvex feature of the studied problem, we may not obtain the global optimal solution. Nevertheless, SPCA iteration can always guarantee the local optimality [20]. As illustrated in the numerical results, the performance of our proposed scheme is remarkably superior to approaches proposed in [10]–[12].

Case $\mu(\theta_3,\theta_4) > \mu(\theta_1,\theta_2)$:

$$S_2(\tilde{\omega}) = \begin{cases} \{q|\chi(\theta_2,\tilde{\omega}) \le \cos\vartheta_q^2 \le \cos\theta_3\}, & -\mu(\theta_1,\theta_3) \le \tilde{\omega} < -\mu(\theta_2,\theta_3) \\ \{q|\chi(\theta_2,\tilde{\omega}) \le \cos\vartheta_q^2 \le \chi(\theta_1,\tilde{\omega})\}, & -\mu(\theta_2,\theta_4) \le \tilde{\omega} < -\mu(\theta_1,\theta_3) \\ \{q|\cos\theta_4 \le \cos\vartheta_q^2 \le \chi(\theta_1,\tilde{\omega})\}, & -\mu(\theta_1,\theta_4) \le \tilde{\omega} \le -\mu(\theta_2,\theta_4) \end{cases} \tag{31-1}$$

Case $\mu(\theta_3,\theta_4) \le \mu(\theta_1,\theta_2)$:

$$S_2(\tilde{\omega}) = \begin{cases} \{q|\chi(\theta_2,\tilde{\omega}) \le \cos\vartheta_q^2 \le \cos\theta_3\}, & -\mu(\theta_2,\theta_4) \le \tilde{\omega} < -\mu(\theta_2,\theta_3) \\ \{q|\cos\theta_4 \le \cos\vartheta_q^2 \le \cos\theta_3\}, & -\mu(\theta_1,\theta_3) \le \tilde{\omega} < -\mu(\theta_2,\theta_4) \\ \{q|\cos\theta_4 \le \cos\vartheta_q^2 \le \chi(\theta_1,\tilde{\omega})\}, & -\mu(\theta_1,\theta_4) \le \tilde{\omega} \le -\mu(\theta_1,\theta_3) \end{cases} \tag{31-2}$$

Case $\mu(\theta_3,\theta_4) > \mu(\theta_1,\theta_2)$:

$$\mathbb{S}_2(\tilde{\omega}) = \begin{cases} \{x|\arccos(\cos\theta_3 - \tilde{\omega}) \le x \le \theta_2\}, & -\mu(\theta_1,\theta_3) \le \tilde{\omega} < -\mu(\theta_2,\theta_3) \\ \{x|\theta_1 \le x \le \theta_2\}, & -\mu(\theta_2,\theta_4) \le \tilde{\omega} < -\mu(\theta_1,\theta_3) \\ \{x|\theta_1 \le x \le \arccos(\cos\theta_4 - \tilde{\omega})\}, & -\mu(\theta_1,\theta_4) \le \tilde{\omega} \le -\mu(\theta_2,\theta_4) \end{cases} \tag{33-1}$$

Case $\mu(\theta_3,\theta_4) \le \mu(\theta_1,\theta_2)$:

$$\mathbb{S}_2(\tilde{\omega}) = \begin{cases} \{x|\arccos(\cos\theta_3 - \tilde{\omega}) \le x \le \theta_2\}, & -\mu(\theta_2,\theta_4) \le \tilde{\omega} < -\mu(\theta_2,\theta_3) \\ \{x|\arccos(\cos\theta_3 - \tilde{\omega}) \le x \le \arccos(\cos\theta_4 - \tilde{\omega})\}, & -\mu(\theta_1,\theta_3) \le \tilde{\omega} < -\mu(\theta_2,\theta_4) \\ \{x|\theta_1 \le x \le \arccos(\cos\theta_4 - \tilde{\omega})\}, & -\mu(\theta_1,\theta_4) \le \tilde{\omega} \le -\mu(\theta_1,\theta_3) \end{cases} \tag{33-2}$$

APPENDIX

First, the index set function $S_2(\tilde{\omega})$ can be rewritten in (31-1) and (31-2), as shown at the top of this page, under two different cases, respectively.

We further define the continuous counterpart of $S_2(\tilde{\omega})$ as:

$$\mathbb{S}_2(\tilde{\omega}) = \{\vartheta|\chi(\theta_2,\tilde{\omega}) \le \cos\vartheta \le \chi(\theta_1,\tilde{\omega}), \cos\theta_3 \le \cos\vartheta \le \cos\theta_4\}. \tag{32}$$

We can further rewrite $\mathbb{S}_2(\tilde{\omega})$ in (33-1) and (33-2), as shown at the top of this page, under two different cases, respectively.

In order to transform the window function $W_2(\tilde{\omega})$ to the integral form, the density function of ϑ which is the continuous counterpart of ϑ_q can be given by $f(\vartheta) = \frac{\sin\vartheta}{\mu(\theta_3,\theta_4)}$. As a result, the window function $W_2(\tilde{\omega})$ can be expressed as

$$\begin{aligned} &W_2(\tilde{\omega}) \\ &= \frac{2\pi}{(\theta_2-\theta_1)Q}\sum_{q=1}^{Q}\frac{1}{\sqrt{1-\chi(\vartheta_q^2,-\tilde{\omega})^2}}\mathcal{I}_q^2(\tilde{\omega}) \\ &= \frac{2\pi}{(\theta_2-\theta_1)}\frac{1}{\mu(\theta_3,\theta_4)}\int_{\theta_3}^{\theta_4}\frac{\sin\vartheta}{\sqrt{1-\chi(\vartheta,-\tilde{\omega})^2}}\mathcal{I}^2(\vartheta,\tilde{\omega})d\vartheta, \end{aligned} \tag{34}$$

where $\mathcal{I}^2(\vartheta,\tilde{\omega})$ corresponds to the continuous version of $\mathcal{I}_q^2(\tilde{\omega})$:

$$\mathcal{I}(\vartheta,\tilde{\omega}) = \begin{cases} 1, & \vartheta \in \mathbb{S}_2(\tilde{\omega}), \\ 0, & \vartheta \notin \mathbb{S}_2(\tilde{\omega}). \end{cases} \tag{35}$$

In order to further simplify (34), we take a variable substitution of $x = \arccos(\cos\vartheta - \tilde{\omega})$, $\vartheta = \arccos(\cos x + \tilde{\omega})$ i.e., then the indicator function $\mathcal{I}^2(\vartheta,\tilde{\omega})$ becomes $\mathcal{I}^2(\arccos(\cos x+\tilde{\omega}),\tilde{\omega})$. The window function $W_2(\tilde{\omega})$ can be transform into

$$\begin{aligned} W_2(\tilde{\omega}) =& \frac{2\pi}{(\theta_2-\theta_1)}\frac{1}{\mu(\theta_3,\theta_4)} \\ &\times\int_{\arccos(\cos\theta_3-\tilde{\omega})}^{\arccos(\cos\theta_4-\tilde{\omega})}\mathcal{I}^2(\arccos(\cos x+\tilde{\omega}),\tilde{\omega})dx. \end{aligned} \tag{36}$$

After the variable substitution, $W_2(\tilde{\omega})$ can be finally expressed in closed-form as (16-1) and (16-2).

REFERENCES

[1] J. Wu and P. Fan, "A survey on high mobility wireless communications: Challenges, opportunities and solutions," *IEEE Access*, vol. 4, pp. 450–476, 2016.

[2] T. Hwang, C. Yang, G. Wu, S. Li, and G. Ye Li, "OFDM and its wireless applications: A survey," *IEEE Trans. Veh. Technol.*, vol. 58, no. 4, pp. 1673–1694, May 2009.

[3] Y. Zhang, Q. Yin, P. Mu, and L. Bai, "Multiple Doppler shifts compensation and ICI elimination by beamforming in high-mobility OFDM systems," in *Proc. 6th Int. ICST Conf. Commun. Netw. China (CHINACOM)*, Aug. 2011, pp. 170–175.

[4] T. L. Marzetta, "Noncooperative cellular wireless with unlimited numbers of base station antennas," *IEEE Trans. Wireless Commun.*, vol. 9, no. 11, pp. 3590–3600, Nov. 2010.

[5] F. Rusek, D. Persson, B. Kiong Lau, E. G. Larsson, T. L. Marzetta, and F. Tufvesson, "Scaling up MIMO: Opportunities and challenges with very large arrays," *IEEE Signal Process. Mag.*, vol. 30, no. 1, pp. 40–60, Jan. 2013.

[6] E. G. Larsson, O. Edfors, F. Tufvesson, and T. L. Marzetta, "Massive MIMO for next generation wireless systems," *IEEE Commun. Mag.*, vol. 52, no. 2, pp. 186–195, Feb. 2014.

[7] L. Lu, G. Y. Li, A. Lee Swindlehurst, A. Ashikhmin, and R. Zhang, "An overview of massive MIMO: Benefits and challenges," *IEEE J. Sel. Topics Signal Process.*, vol. 8, no. 5, pp. 742–758, Oct. 2014.

[8] W. Zhang, F. Gao, S. Jin, and H. Lin, "Frequency synchronization for uplink massive MIMO systems," *IEEE Trans. Wireless Commun.*, vol. 17, no. 1, pp. 235–249, Jan. 2018.

[9] W. Guo, W. Zhang, P. Mu, F. Gao, and B. Yao, "Angle–domain Doppler pre–compensation for high–mobility OFDM uplink with massive ULA," in *Proc. GLOBECOM IEEE Global Commun. Conf.*, Dec. 2017, pp. 1–6.
[10] W. Guo, W. Zhang, P. Mu, F. Gao, and H. Lin, "High–mobility wideband massive MIMO communications: Doppler compensation, analysis and scaling laws," *IEEE Trans. Wireless Commun.*, vol. 18, no. 6, pp. 3177–3191, Jun. 2019.
[11] Y. Ge, W. Zhang, F. Gao, S. Zhang, and X. Ma, "Beamforming network optimization for reducing channel time variation in high–mobility massive MIMO," *IEEE Trans. Commun.*, vol. 67, no. 10, pp. 6781–6795, Oct. 2019.
[12] Z. Hu and W. Zhang, "Radiation efficiency aware high–mobility massive MIMO with antenna selection," *IEEE Trans. Veh. Technol.*, vol. 68, no. 11, pp. 11363–11367, Nov. 2019.
[13] K. Zheng, L. Zhao, J. Mei, B. Shao, W. Xiang, and L. Hanzo, "Survey of large–scale MIMO systems," *IEEE Commun. Surveys Tuts.*, vol. 17, no. 3, pp. 1738–1760, Apr. 2015.
[14] Q. Wang, D. Jiang, G. Liu, and Z. Yan, "Coordinated multiple points transmission for LTE–advanced systems," in *Proc. 5th Int. Conf. Wireless Commun., Netw. Mobile Comput.*, Beijing, China, Sep. 2009, pp. 1–4.
[15] F. Huang, Y. Wang, J. Geng, and D. Yang, "Antenna mismatch and calibration problem in coordinated multi-point transmission system," *IET Commun.*, vol. 6, no. 3, p. 289, 2012.
[16] W. Luo, R. Zhang, and X. Fang, "A CoMP soft handover scheme for LTE systems in high speed railway," *EURASIP J. Wireless Commun. Netw.*, vol. 2012, Jun. 2012, Art. no. 196.
[17] S. Mosleh, L. Liu, and J. Zhang, "Proportional–fair resource allocation for coordinated multi–point transmission in LTE–advanced," *IEEE Trans. Wireless Commun.*, vol. 15, no. 8, pp. 5355–5367, Aug. 2016.
[18] S. Liu, P.-C. Peng, C.-W. Hsu, J. He, H. Tian, and G.-K. Chang, "An artificial neural network MIMO demultiplexer for small–cell MM–wave RoF coordinated multi–point transmission system," in *Proc. Eur. Conf. Opt. Commun.(ECOC)*, Sep. 2018, pp. 1–3.
[19] C.-W. Chen, H.-W. Tsao, and P.-Y. Tsai, "MIMO precoder design with a compensated QR–decomposition combination for CoMP downlink scenarios," *IEEE Trans. Veh. Technol.*, vol. 65, no. 10, pp. 7982–7992, Oct. 2016.
[20] A. Beck, A. Ben-Tal, and L. Tetruashvili, "A sequential parametric convex approximation method with applications to nonconvex truss topology design problems," *J. Global Optim.*, vol. 47, no. 1, pp. 29–51, May 2010.
[21] Y. Cheng and M. Pesavento, "Joint optimization of source power allocation and distributed relay beamforming in multiuser peer-to-peer relay networks," *IEEE Trans. Signal Process.*, vol. 60, no. 6, pp. 2962–2973, Jun. 2012.
[22] Y. Zheng and C. Xiao, "Simulation models with correct statistical properties for Rayleigh fading channels," *IEEE Trans. Commun.*, vol. 51, no. 6, pp. 920–928, Jun. 2003.

ZHINAN HU received the B.S. degree from the School of Electronical Information Science and Technology, Xiamen University, Xiamen, China, in 2017. She is currently pursuing the master's degree with the Ministry of Education Key Laboratory for Intelligent Networks and Network Security, Xi'an Jiaotong University. She was with the School of Electronic and Information Engineering, Xi'an Jiaotong University. Her research interests include high-mobility wireless communications, MIMO, and array signal processing.

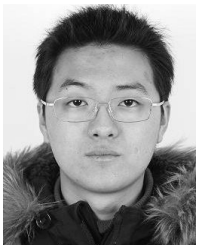

WEILE ZHANG received the B.S. and Ph.D. degrees in information and communication engineering from Xi'an Jiaotong University, Xi'an, China, in 2006 and 2012, respectively. From October 2010 to October 2011, he was a Visiting Scholar with the Department of Computer Science, University of California, Santa Barbara, CA, USA. He is currently an Associate Professor with the Ministry of Education Key Laboratory for Intelligent Networks and Network Security, Xi'an Jiaotong University. His research interests include broadband wireless communications, MIMO, array signal processing, and localization in wireless networks.